EUROPEAN ORGANISATION FOR NUCLEAR RESEARCH

CERN-PPE/96-132
September 27, 1996

# Inclusive Jet Production in Photon-Photon Collisions at $\sqrt{s_{ee}} = 130$ and 136 GeV

The OPAL Collaboration

Abstract

The inclusive one- and two-jet production cross-sections are measured in collisions of quasi-real photons radiated from the LEP beams at $e^+e^-$ centre-of-mass energies $\sqrt{s}_{ee} = 130$ and 136 GeV using the OPAL detector at LEP. Hard jets are reconstructed using a cone jet finding algorithm. The differential jet cross-sections $d\sigma/dE_T^{jet}$ are compared to next-to-leading order perturbative QCD calculations. Transverse energy flows in jets are studied separately for direct and resolved two-photon events.

(Submitted to Zeitschrift für Physik)

# The OPAL Collaboration


K. Ackerstaff[8], G. Alexander[23], J. Allison[16], N. Altekamp[5], K. Ametewee[25], K.J. Anderson[9], S. Anderson[12], S. Arcelli[2], S. Asai[24], D. Axen[29], G. Azuelos[18,a], A.H. Ball[17], E. Barberio[8], R.J. Barlow[16], R. Bartoldus[3], J.R. Batley[5], J. Bechtluft[14], C. Beeston[16], T. Behnke[8], A.N. Bell[1], K.W. Bell[20], G. Bella[23], S. Bentvelsen[8], P. Berlich[10], S. Bethke[14], O. Biebel[14], V. Blobel[27], I.J. Bloodworth[1], J.E. Bloomer[1], M. Bobinski[10], P. Bock[11], H.M. Bosch[11], M. Boutemeur[34], B.T. Bouwens[12], S. Braibant[12], R.M. Brown[20], H.J. Burckhart[8], C. Burgard[8], R. Bürgin[10], P. Capiluppi[2], R.K. Carnegie[6], A.A. Carter[13], J.R. Carter[5], C.Y. Chang[17], D.G. Charlton[1,b], D. Chrisman[4], P.E.L. Clarke[15], I. Cohen[23], J.E. Conboy[15], O.C. Cooke[16], M. Cuffiani[2], S. Dado[22], C. Dallapiccola[17], G.M. Dallavalle[2], S. De Jong[12], L.A. del Pozo[8], K. Desch[3], M.S. Dixit[7], E. do Couto e Silva[12], M. Doucet[18], E. Duchovni[26], G. Duckeck[34], I.P. Duerdoth[16], J.E.G. Edwards[16], P.G. Estabrooks[6], H.G. Evans[9], M. Evans[13], F. Fabbri[2], P. Fath[11], F. Fiedler[27], M. Fierro[2], H.M. Fischer[3], R. Folman[26], D.G. Fong[17], M. Foucher[17], A. Fürtjes[8], P. Gagnon[7], A. Gaidot[21], J.W. Gary[4], J. Gascon[18], S.M. Gascon-Shotkin[17], N.I. Geddes[20], C. Geich-Gimbel[3], F.X. Gentit[21], T. Geralis[20], G. Giacomelli[2], P. Giacomelli[4], R. Giacomelli[2], V. Gibson[5], W.R. Gibson[13], D.M. Gingrich[30,a], D. Glenzinski[9], J. Goldberg[22], M.J. Goodrick[5], W. Gorn[4], C. Grandi[2], E. Gross[26], J. Grunhaus[23] M. Gruwé[8], C. Hajdu[32], G.G. Hanson[12], M. Hansroul[8], M. Hapke[13], C.K. Hargrove[7], P.A. Hart[9], C. Hartmann[3], M. Hauschild[8], C.M. Hawkes[5], R. Hawkings[8], R.J. Hemingway[6], M. Herndon[17], G. Herten[10], R.D. Heuer[8], M.D. Hildreth[8], J.C. Hill[5], S.J. Hillier[1], T. Hilse[10], P.R. Hobson[25], R.J. Homer[1], A.K. Honma[28,a], D. Horváth[32,c], R. Howard[29], R.E. Hughes-Jones[16], D.E. Hutchcroft[5], P. Igo-Kemenes[11], D.C. Imrie[25], M.R. Ingram[16], K. Ishii[24], A. Jawahery[17], P.W. Jeffreys[20], H. Jeremie[18], M. Jimack[1], A. Joly[18], C.R. Jones[5], G. Jones[16], M. Jones[6], R.W.L. Jones[8], U. Jost[11], P. Jovanovic[1], T.R. Junk[8], D. Karlen[6], K. Kawagoe[24], T. Kawamoto[24], R.K. Keeler[28], R.G. Kellogg[17], B.W. Kennedy[20], B.J. King[8], J. Kirk[29], S. Kluth[8], T. Kobayashi[24], M. Kobel[10], D.S. Koetke[6], T.P. Kokott[3], M. Kolrep[10], S. Komamiya[24], T. Kress[11], P. Krieger[6], J. von Krogh[11], P. Kyberd[13], G.D. Lafferty[16], H. Lafoux[21], R. Lahmann[17], W.P. Lai[19], D. Lanske[14], J. Lauber[15], S.R. Lautenschlager[31], J.G. Layter[4], D. Lazic[22], A.M. Lee[31], E. Lefebvre[18], D. Lellouch[26], J. Letts[2], L. Levinson[26], C. Lewis[15], S.L. Lloyd[13], F.K. Loebinger[16], G.D. Long[17], M.J. Losty[7], J. Ludwig[10], A. Malik[21], M. Mannelli[8], S. Marcellini[2], C. Markus[3], A.J. Martin[13], J.P. Martin[18], G. Martinez[17], T. Mashimo[24], W. Matthews[25], P. Mättig[3], W.J. McDonald[30], J. McKenna[29], E.A. Mckigney[15], T.J. McMahon[1], A.I. McNab[13], R.A. McPherson[8], F. Meijers[8], S. Menke[3], F.S. Merritt[9], H. Mes[7], J. Meyer[27], A. Michelini[2], G. Mikenberg[26], D.J. Miller[15], R. Mir[26], W. Mohr[10], A. Montanari[2], T. Mori[24], M. Morii[24], U. Müller[3], K. Nagai[26], I. Nakamura[24], H.A. Neal[8], B. Nellen[3], B. Nijjhar[16], R. Nisius[8], S.W. O'Neale[1], F.G. Oakham[7], F. Odorici[2], H.O. Ogren[12], N.J. Oldershaw[16], T. Omori[24], M.J. Oreglia[9], S. Orito[24], J. Pálinkás[33,d], G. Pásztor[32], J.R. Pater[16], G.N. Patrick[20], J. Patt[10], M.J. Pearce[1], S. Petzold[27], P. Pfeifenschneider[14], J.E. Pilcher[9], J. Pinfold[30], D.E. Plane[8], P. Poffenberger[28], B. Poli[2], A. Posthaus[3], H. Przysiezniak[30], D.L. Rees[1], D. Rigby[1], S. Robertson[28], S.A. Robins[13], N. Rodning[30], J.M. Roney[28], A. Rooke[15], E. Ros[8], A.M. Rossi[2], M. Rosvick[28], P. Routenburg[30], Y. Rozen[22], K. Runge[10], O. Runolfsson[8], U. Ruppel[14], D.R. Rust[12], R. Rylko[25], K. Sachs[10], E.K.G. Sarkisyan[23], M. Sasaki[24], C. Sbarra[2], A.D. Schaile[34], O. Schaile[34], F. Scharf[3], P. Scharff-Hansen[8], P. Schenk[27], B. Schmitt[8], S. Schmitt[11], M. Schröder[8], H.C. Schultz-Coulon[10], M. Schulz[8], M. Schumacher[3], P. Schütz[3], W.G. Scott[20], T.G. Shears[16], B.C. Shen[4], C.H. Shepherd-Themistocleous[8], P. Sherwood[15], G.P. Siroli[2], A. Sittler[27], A. Skillman[15], A. Skuja[17], A.M. Smith[8], T.J. Smith[28], G.A. Snow[17], R. Sobie[28],

S. Söldner-Rembold[10], R.W. Springer[30], M. Sproston[20], A. Stahl[3], M. Steiert[11], K. Stephens[16], J. Steuerer[27], B. Stockhausen[3], D. Strom[19], F. Strumia[8], P. Szymanski[20], R. Tafirout[18], S.D. Talbot[1], S. Tanaka[24], P. Taras[18], S. Tarem[22], M. Thiergen[10], M.A. Thomson[8], E. von Törne[3], S. Towers[6], I. Trigger[18], T. Tsukamoto[24], E. Tsur[23], A.S. Turcot[9], M.F. Turner-Watson[8], P. Utzat[11], R. Van Kooten[12], G. Vasseur[21], M. Verzocchi[10], P. Vikas[18], M. Vincter[28], E.H. Vokurka[16], F. Wäckerle[10], A. Wagner[27], C.P. Ward[5], D.R. Ward[5], J.J. Ward[15], P.M. Watkins[1], A.T. Watson[1], N.K. Watson[7], P.S. Wells[8], N. Wermes[3], J.S. White[28], B. Wilkens[10], G.W. Wilson[27], J.A. Wilson[1], G. Wolf[26], S. Wotton[5], T.R. Wyatt[16], S. Yamashita[24], G. Yekutieli[26], V. Zacek[18],

[1]School of Physics and Space Research, University of Birmingham, Birmingham B15 2TT, UK
[2]Dipartimento di Fisica dell' Università di Bologna and INFN, I-40126 Bologna, Italy
[3]Physikalisches Institut, Universität Bonn, D-53115 Bonn, Germany
[4]Department of Physics, University of California, Riverside CA 92521, USA
[5]Cavendish Laboratory, Cambridge CB3 0HE, UK
[6] Ottawa-Carleton Institute for Physics, Department of Physics, Carleton University, Ottawa, Ontario K1S 5B6, Canada
[7]Centre for Research in Particle Physics, Carleton University, Ottawa, Ontario K1S 5B6, Canada
[8]CERN, European Organisation for Particle Physics, CH-1211 Geneva 23, Switzerland
[9]Enrico Fermi Institute and Department of Physics, University of Chicago, Chicago IL 60637, USA
[10]Fakultät für Physik, Albert Ludwigs Universität, D-79104 Freiburg, Germany
[11]Physikalisches Institut, Universität Heidelberg, D-69120 Heidelberg, Germany
[12]Indiana University, Department of Physics, Swain Hall West 117, Bloomington IN 47405, USA
[13]Queen Mary and Westfield College, University of London, London E1 4NS, UK
[14]Technische Hochschule Aachen, III Physikalisches Institut, Sommerfeldstrasse 26-28, D-52056 Aachen, Germany
[15]University College London, London WC1E 6BT, UK
[16]Department of Physics, Schuster Laboratory, The University, Manchester M13 9PL, UK
[17]Department of Physics, University of Maryland, College Park, MD 20742, USA
[18]Laboratoire de Physique Nucléaire, Université de Montréal, Montréal, Quebec H3C 3J7, Canada
[19]University of Oregon, Department of Physics, Eugene OR 97403, USA
[20]Rutherford Appleton Laboratory, Chilton, Didcot, Oxfordshire OX11 0QX, UK
[21]CEA, DAPNIA/SPP, CE-Saclay, F-91191 Gif-sur-Yvette, France
[22]Department of Physics, Technion-Israel Institute of Technology, Haifa 32000, Israel
[23]Department of Physics and Astronomy, Tel Aviv University, Tel Aviv 69978, Israel
[24]International Centre for Elementary Particle Physics and Department of Physics, University of Tokyo, Tokyo 113, and Kobe University, Kobe 657, Japan
[25]Brunel University, Uxbridge, Middlesex UB8 3PH, UK
[26]Particle Physics Department, Weizmann Institute of Science, Rehovot 76100, Israel
[27]Universität Hamburg/DESY, II Institut für Experimental Physik, Notkestrasse 85, D-22607 Hamburg, Germany
[28]University of Victoria, Department of Physics, P O Box 3055, Victoria BC V8W 3P6, Canada

[29]University of British Columbia, Department of Physics, Vancouver BC V6T 1Z1, Canada
[30]University of Alberta, Department of Physics, Edmonton AB T6G 2J1, Canada
[31]Duke University, Dept of Physics, Durham, NC 27708-0305, USA
[32]Research Institute for Particle and Nuclear Physics, H-1525 Budapest, P O Box 49, Hungary
[33]Institute of Nuclear Research, H-4001 Debrecen, P O Box 51, Hungary
[34]Ludwigs-Maximilians-Universität München, Sektion Physik, Am Coulombwall 1, D-85748 Garching, Germany

[a] and at TRIUMF, Vancouver, Canada V6T 2A3
[b] and Royal Society University Research Fellow
[c] and Institute of Nuclear Research, Debrecen, Hungary
[d] and Department of Experimental Physics, Lajos Kossuth University, Debrecen, Hungary

# 1 Introduction

The interaction of two photons in $e^+e^-$ colliders proceeds via the emission of a photon by both beam electrons[1]. Most of the electrons are scattered at very small angles with respect to the beam direction. If both scattered electrons are not detected ("anti-tagged"), the squared four-momenta $Q^2$ carried by the two photons are small and the photons can be considered to be quasi-real ($Q^2 \approx 0$).

The production of hard jets in $\gamma\gamma$ collisions is a tool for the study of the structure of the photon and its interactions, in a way which is complementary to deep inelastic $e\gamma$ scattering [1]. By measuring jet cross-sections in $\gamma\gamma$ interactions, predictions of perturbative QCD and different parametrisations of the photon structure function can be tested. In the Quark Parton Model (QPM) jets are produced by the interaction of bare photons, $\gamma\gamma \to q\overline{q}$. This is called the direct process. The largest part of the total cross-section, however, is modelled by interactions where the photon fluctuates into a hadronic state. The processes are called single-resolved if one photon couples directly to a parton in the other photon and double-resolved if partons from both photons interact [2].

Recently the inclusive one-jet cross-section for the process $\gamma\gamma \to$ jet + X [3, 4] and the inclusive two-jet cross-section for the process $\gamma\gamma \to$ jet + jet + X [4] have been calculated in next-to-leading order (NLO) QCD. These calculations have been compared to measurements at an $e^+e^-$ centre-of-mass energy of $\sqrt{s}_{ee} = 58$ GeV by AMY [5] and TOPAZ [6] for jet transverse momenta between 2.5 and 8.0 GeV/$c$. In addition, a new generation of Monte Carlo generators has become available for the simulation of $\gamma\gamma$ interactions. The generators PYTHIA [7] and PHOJET [8] are based on leading order (LO) QCD calculations.

At the centre-of-mass energy $\sqrt{s}_{ee} = 91.2$ GeV, hadron and jet production in $\gamma\gamma$ interactions at LEP have been published by DELPHI [9] and by ALEPH [10]. In this paper, jet production in $\gamma\gamma$ interactions is measured at $\sqrt{s}_{ee}$ of 130 and 136 GeV in a kinematic regime where the methods of perturbative QCD can be applied. At this energy, the total cross-section for $\gamma\gamma$ interactions is about two orders of magnitude larger than the $e^+e^-$ annihilation cross-section. Background from $e^+e^-$ annihilations at the beam energy or from radiative returns to the $Z^0$ ($e^+e^- \to Z^0\gamma$) is therefore expected to be small.

We present the first study using a cone jet finding algorithm of multi-jet production in two-photon interactions at LEP. The data were collected with the OPAL detector in 1995 and correspond to an integrated luminosity of 4.9 pb$^{-1}$. In Section 2, the kinematic variables are introduced. The Monte Carlo simulations are described in Section 3. A brief account of the OPAL detector and the event selection is given in Section 4. The cone jet finding algorithm is described in Section 5. Transverse energy flows are studied in Section 6. In Section 7, the measured jet cross-sections are compared to NLO calculations. Conclusions are given in Section 8.

[1] Positrons are also referred to as electrons.

# 2 Kinematics

The kinematics of the $\gamma\gamma$ process [11] at a given $\sqrt{s}_{ee}$ are described by the negative square of the four-momentum transfers, $Q_i^2 = -q_i^2$, carried by the two ($i = 1,2$) photons and by the square of the invariant mass of the hadronic final state, $W^2 = s_{\gamma\gamma} = (q_1 + q_2)^2$. A schematic diagram of a two-photon process is shown in Fig. 1.

Each $Q_i^2$ is related to the electron scattering angle $\Theta_i'$ relative to the beam direction by

$$Q_i^2 = -(p_i - p_i')^2 \approx 2E_iE_i'(1 - \cos\Theta_i'), \tag{1}$$

where $p_i$ and $p_i'$ are the four-momenta of the beam electrons and the scattered electrons, respectively, and $E_i$ and $E_i'$ are their energies. Events with detected scattered electrons are excluded from the analysis. This anti-tagging condition defines an upper limit on $Q^2$ for both photons. $W^2$ is determined from the energies and momenta of the final state hadrons,

$$W^2 = \left(\sum_h E_h\right)^2 - \left(\sum_h \vec{p}_h\right)^2,$$

where the sums, $\sum_h$, run over all measured particles. The spectrum of photons with an energy fraction $y$ of the electron beam may be obtained by the Equivalent Photon Approximation (EPA) [12]:

$$f_{\gamma/e}(y) = \frac{\alpha}{2\pi}\frac{1+(1-y)^2}{y}\log\frac{Q^2_{\max}}{Q^2_{\min}} - 2m_e^2 y\left(\frac{1}{Q^2_{\min}} - \frac{1}{Q^2_{\max}}\right)$$

with $\alpha$ being the electromagnetic coupling constant. The minimum kinematically allowed squared four-momentum transfer $Q^2_{\min}$ is determined by the electron mass $m_e$:

$$Q^2_{\min} = \frac{m_e^2 y^2}{1-y}.$$

The effective maximum four-momentum transfer $Q^2_{\max}$ is given by the anti-tagging condition, i. e. the case where both electrons remain undetected. This condition is met when the scattering angle $\Theta'$ of the electrons is less than $\Theta_{\max}$, where $\Theta_{\max}$ is the angle between the beam-axis and the inner edge of the detector.

# 3 Monte Carlo simulation

The Monte Carlo generators PYTHIA 5.721 [7,13] and PHOJET 1.05 [8] are used, both based on LO QCD calculations. These generators, which have been optimised to describe $\gamma$p and $\overline{\text{p}}$p interactions, are used for the first time in an experimental analysis to study the hadronic final state in $\gamma\gamma$ interactions. The probability of finding a parton in the photon is taken from parametrisations of the parton distribution functions. The SaS-1D parametrisation [14] is used in PYTHIA and the leading order GRV parametrisation [15] in PHOJET. All possible hard interactions of quarks, gluons and photons are simulated using LO matrix elements for massless quarks. The final state quarks are subsequently put on mass-shell. Both generators allow multiple parton interactions. The fragmentation of the parton final state is handled in

both generators by the routines of JETSET 7.408 [7]. Initial and final state parton radiation is included based on the leading logarithm approximation.

The two-photon mode of PYTHIA simulates the interactions of real photons with $Q^2 = 0$. The virtuality of the photons defined by $Q^2$ enters only through the EPA in the generation of the photon energy spectrum, but the electrons are scattered at zero angle. The $\gamma\gamma$ interactions are subdivided into six different event classes (Fig. 2). These classes correspond to all possible combinations of the photon components [13]:

- Direct: the interaction of the bare photon;
- Vector Meson Dominance (VMD): the photon turns into a meson;
- Anomalous: the photon splits into a $q\bar{q}$ pair of high virtuality.

The VMD and anomalous component together can be identified with the resolved photon, which leads to the classifications direct (Fig. 2a), single-resolved (Fig. 2b–c) and double-resolved (Fig. 2d–f). In addition to the hard processes, soft processes such as, for example, elastic or diffractive scattering, are also generated. The total, elastic and diffractive cross-sections are taken from Regge models.

The PHOJET generator is based on the Dual Parton Model (DPM) combined with perturbative QCD. The total cross-sections are obtained from fitting a Regge parametrisation to pp, $\overline{\mathrm{p}}\mathrm{p}$ and $\gamma\mathrm{p}$ data. The transition from hard to soft interactions is defined by the transverse momentum of the partons.

In PHOJET, both direct and resolved interactions are taken into account. The anomalous component and the VMD component are included in the resolved cross-section through the definition of the parton distribution functions. The $Q^2$ suppression of the total $\gamma\gamma$ cross-section is parametrised using GVMD (Generalised Vector Meson Dominance). The $Q^2$ dependent transverse momentum of the scattered electrons is taken into account in the simulation of the hadronic final state, which is otherwise simulated in the same way as for real photons.

The backgrounds from $\mathrm{e^+e^-}$ annihilation events are generated with PYTHIA 5.720 [7] for the process $\mathrm{e^+e^-} \to (\gamma/\mathrm{Z^0})^* \to q\overline{q}(\gamma)$ and with KORALZ 4.0 [16] for the process $\mathrm{e^+e^-} \to (\gamma/\mathrm{Z^0})^* \to \tau^+\tau^-(\gamma)$. The process $\mathrm{e^+e^-} \to \mathrm{e^+e^-}\tau^+\tau^-$, which is also considered to be background, is simulated with the Vermaseren generator [17], and single-tagged $\mathrm{e}\gamma$ events with PYTHIA 5.721. In single-tagged events, one of the two scattered electrons is detected. All Monte Carlo samples were generated with full simulation of the OPAL detector [18]. They are analysed using the same reconstruction algorithms as are applied to the data.

# 4 The OPAL detector and event selection

A detailed description of the OPAL detector can be found in Reference [19], and therefore only a brief account of the main features relevant to the present analysis will be given here.

The central tracking systems are located inside a solenoidal magnet which provides a uniform axial magnetic field of 0.435 T along the beam axis[2]. The magnet is surrounded by a lead glass electromagnetic calorimeter (ECAL) and a hadronic calorimeter (HCAL) of the sampling type. Outside the HCAL, the detector is surrounded by a system of muon chambers. There are similar layers of detectors in the forward and backward endcaps.

The main tracking detector is the central jet chamber. It has 24 sectors with radial planes of 159 sense wires spaced by 1 cm. The transverse momenta $p_T$ of tracks are measured with a precision parametrised by $\sigma_{p_T}/p_T = \sqrt{0.02^2 + (0.0015 \cdot p_T)^2}$ ($p_T$ in GeV/$c$) for $|\cos\theta| < 0.73$.

The ECAL has barrel and endcap sections, both constructed from lead glass blocks with a depth of 24.6 radiation lengths in the barrel and more than 22 radiation lengths in the endcaps. The endcaps cover the angular range from 200 to 630 mrad.

The forward calorimeters consist of cylindrical lead-scintillator calorimeters with a depth of 24 radiation lengths divided azimuthally into 16 segments. The electromagnetic energy resolution is about $18\%/\sqrt{E}$, where $E$ is in GeV. The acceptance of the forward calorimeters covers the angular range from 47 to 140 mrad from the beam direction.

The silicon tungsten detectors [20] at each end of the OPAL detector cover an angular region between 25 and 59 mrad in front of the forward calorimeters. Each calorimeter consists of 19 layers of silicon detectors and 18 layers of tungsten, corresponding to a total of 22 radiation lengths. Each silicon layer consists of 16 wedge shaped silicon detectors. The electromagnetic energy resolution is about $25\%/\sqrt{E}$ ($E$ in GeV).

Two-photon events are selected with the following set of cuts:

- The sum of all energy deposits in the ECAL, the HCAL and the forward calorimeters has to be less than 50 GeV.
- The visible invariant hadronic mass, $W_{\mathrm{ECAL}}$, measured in the ECAL has to be greater than 3 GeV.
- The missing transverse energy of the event measured in the ECAL and the forward calorimeters has to be less than 5 GeV.
- At least 5 tracks must have been found in the tracking chambers. A track is required to have a minimum transverse momentum with respect to the $z$ axis of 50 MeV/$c$, more than 20 hits in the central jet chamber, and the innermost hit of the track must be inside a radius of 60 cm with respect to the $z$ axis. The point of closest approach to the beam spot must be less than 30 cm in the $z$ direction and less than 2 cm in the $r\phi$ plane. For the polar angle $\theta$ of the track, we require $|\cos\theta| < 0.964$.
- No track in the event has a momentum greater than 15 GeV/$c$.

[2]In the OPAL coordinate system the $x$ axis points towards the centre of the LEP ring, the $y$ axis points upwards and the $z$ axis points in the direction of the electron beam. The polar angle $\theta$, the azimuthal angle $\phi$ and the radius $r$ denote the usual spherical coordinates.

- To remove events with scattered electrons in the forward or in the silicon tungsten calorimeters, the total energy sum measured in the forward calorimeters has to be less than 40 GeV and the total energy sum measured in the silicon tungsten calorimeters less than 20 GeV. This cut corresponds to an effective maximum value of the four-momentum transfer $Q^2_{\rm max} \approx 0.8$ GeV$^2$ as can be verified based on Eq. 1 with 66.5 GeV average beam energy (anti-tagging condition).

In order to estimate the $z$ position of the vertex, even for low multiplicity events, we calculate the weighted average $\langle z_0 \rangle$ of the $z$ coordinates of all tracks at the point of closest approach to the origin in the $r\phi$ plane using

$$\langle z_0 \rangle = \frac{\sum_i z_i \,/\, \sigma^2_{zi}}{\sum_i 1 \,/\, \sigma^2_{z\,i}},$$

where $\sigma_{z_i}$ is the measurement error on $z_i$. The background due to beam-gas or beam-wall interactions is reduced by requiring $|\langle z_0 \rangle| < 10$ cm and $|Q| \leq 3$, where $Q$ is the net charge of an event calculated from adding the charges of all tracks.

We use data corresponding to an integrated luminosity of 4.9 pb$^{-1}$. After applying all cuts 7808 events remain, 48 % of them at 65 GeV beam energy and 52 % at 68 GeV. The visible hadronic invariant mass $W_{\rm vis}$ is measured using the electromagnetic and hadronic calorimeters, the forward and silicon tungsten calorimeters, and all tracks. The $W_{\rm vis}$ distribution shown in Fig. 3 for all selected events is well described by the Monte Carlo simulations. The average $W_{\rm vis}$ is about 18 GeV in data and about 17 GeV in the Monte Carlo, while in the Monte Carlo events, the average generated invariant mass $W$ for the same events is about 24 GeV.

# 5 Jet reconstruction and backgrounds

The cone jet finding algorithm is used in this paper, since it is expected that jets from $\gamma\gamma$ interactions are similar to cone jets in $\overline{\rm p}$p scattering [21] and in $\gamma$p scattering [22,23]. Recently the cone jet finding algorithm has also been applied in $\rm e^+e^-$ annihilation [24]. The NLO corrections to the jet cross-sections in $\gamma\gamma$ interactions are also calculated within the cone scheme [4].

A jet is defined as a set of particles[3] whose momenta lie within a cone of size $R$, such that the axis of the cone coincides with the momentum sum of the particles contained. The cone size $R$ is defined as

$$R = \sqrt{(\Delta\eta)^2 + (\Delta\phi)^2},$$

with $\eta = -\ln\tan(\theta/2)$ being the pseudorapidity and $\phi$ the azimuthal angle in the laboratory frame in radians. $\Delta\eta$ and $\Delta\phi$ are the differences between the cone axis and the particle direction. The total transverse energy $E_T^{\rm jet}$ of the jet inside the cone is the scalar sum of the transverse energies of its components,

$$E_T^{\rm jet} = \sum_i E_{T_i}.$$

[3]The cone jet finding algorithm can be applied to partons or hadrons generated in a QCD Monte Carlo program, or to tracks and calorimeter clusters observed in the OPAL detector. In the description of the algorithm they are generally referred to as "particles".

The transverse energy $E_{T_i}$ of a particle is defined relative to the $z$ axis of the detector throughout this paper with $E_{T_i} = E_i \sin\theta_i$. The value of $E_T^{\rm jet}$ must be greater than $E_T^{\rm min}$. Thus the results of the cone jet finding algorithm depend on two parameters, the cone size $R$ and $E_T^{\rm min}$, here chosen to be $R = 1$ and $E_T^{\rm min} = 2$ GeV. In addition, a procedure has been defined in case particles are assigned to more than one jet. The jet finding procedure is described in detail in Reference [24] for jets in $e^+e^-$ annihilations, where the total energy is used instead of the transverse energy.

Tracks measured in the tracking chambers and clusters measured in the ECAL and HCAL are used in the cone jet finding algorithm. To avoid double counting of particle momenta, a matching algorithm is applied. If a cluster is associated with a charged track, the cluster energy and the energy of the track are compared. Here $f(\vec{p})$ is the expected energy response of the calorimeters for a charged track with momentum $\vec{p}$. To calculate the energy of a charged track the pion mass is assumed. The cluster is rejected if the energy of the cluster is less than expected from the track energy. If the cluster energy exceeds the expected energy plus a certain tolerance, the energy of the cluster is reduced to $E - f(\vec{p})$. In this case the track momentum and the reduced energy of the cluster are taken separately.

The geometrical acceptance of the ECAL and HCAL and of the tracking chambers is restricted to the region $|\eta| \lesssim 2$. The jet direction in the laboratory frame is therefore required to be within $|\eta^{\rm jet}| < 1$. The pseudorapidity $\eta^{\rm jet}$ and the azimuthal angle $\phi^{\rm jet}$ are defined as the sum over the pseudorapidities $\eta_i$ and the azimuthal angles $\phi_i$ of the jet components weighted by their transverse energies $E_{T_i}$:

$$\eta^{\rm jet} = \frac{\sum_i E_{T_i}\eta_i}{\sum_i E_{T_i}} \quad \text{and} \quad \phi^{\rm jet} = \frac{\sum_i E_{T_i}\phi_i}{\sum_i E_{T_i}}.$$

All results are given for jets with $E_T^{\rm jet} > 3$ GeV. This reduces the contribution from soft processes. In PYTHIA, less than 2 % of all generated hadron jets with $E_T^{\rm jet} > 3$ GeV originate from soft processes[4].

About 80 % of all generated Monte Carlo events with at least one hadron jet in the range $E_T^{\rm jet} > 3$ GeV and $|\eta^{\rm jet}| < 1$ are selected. The trigger efficiency for all selected Monte Carlo events which have in addition at least one reconstructed jet in the detector is close to 100 %.

The number of background events is small, about 1 % in total. The numbers of events with different jet multiplicities found in the data after all cuts are given in Table 1, together with the contributions of the main background processes, $\gamma\gamma \to \tau\tau$, $e\gamma \to e$ + hadrons, $e^+e^- \to (\gamma/Z^0)^* \to$ hadrons($\gamma$) and $e^+e^- \to (\gamma/Z^0)^* \to \tau^+\tau^-(\gamma)$, as determined by the Monte Carlo simulations. Less than 1 % of the selected events are single-tagged $e\gamma$ events with $Q^2 > 0.8$ GeV$^2$. The errors on the background are the statistical errors of the Monte Carlo samples. The background from beam-gas and beam-wall interactions is estimated to be negligible, based on the distribution of the vertex position $\langle z_0 \rangle$ and the net charge $Q$ of the events.

[4]PYTHIA process numbers $91 \leq$ ISUB $\leq 96$ [7].

# 6 Energy flow in jet events

In leading order QCD, neglecting multiple parton interactions, two hard parton jets are produced in $\gamma\gamma$ interactions. In single- or double-resolved interactions, the two hard parton jets are expected to be accompanied by one or two remnant jets.

Figures 4a and b show the transverse energy flows

$$\frac{1}{N_{\rm jet}}\frac{{\rm d}E_T}{{\rm d}(\Delta\eta)} \quad \text{and} \quad \frac{1}{N_{\rm jet}}\frac{{\rm d}E_T}{{\rm d}(\Delta\phi)} \tag{2}$$

with respect to the jet direction for all jets. No correction for acceptance or resolution effects has been applied. All tracks and clusters that are used for the jet finding algorithm are included, with

$$\Delta\eta = \eta - \eta^{\rm jet} \ \text{ and } \ \Delta\phi = \phi - \phi^{\rm jet}.$$

The transverse energy $E_T$ of the tracks and clusters is defined, as always, with respect to the $z$ axis of the detector. The energy flow is integrated over $|\Delta\phi| < \pi/2$ for the $\Delta\eta$ projection and over $|\Delta\eta| < 1$ for the $\Delta\phi$ projection. The shape of the selected jet is seen clearly in both $\Delta\eta$ and $\Delta\phi$. The $\Delta\phi$ plot also has a weaker peak at $\Delta\phi = \pm\pi$, as expected if there is a contribution from two-jet events. This effect is also seen for events where the second jet is not reconstructed. Both Monte Carlo models describe the transverse energy flow reasonably well, except for an underestimate in the central region around the jet axis. Nevertheless the overall modelling is sufficiently good to justify using the Monte Carlo models for unfolding the detector resolution effects in the jet cross-section measurements.

In addition to the jet energy flow contained in the cone of size $R = 1$, we expect additional activity due to the photon remnant in resolved photon interactions. In Fig. 4, an underlying constant transverse energy flow (pedestal) is observed which could indicate the existence of such a photon remnant. Its influence can only be studied reliably by using events with two reconstructed jets, since for one-jet events, effects due to a second, unreconstructed, jet cannot be separated from the energy flow created by the photon remnant.

In $\gamma$p events at HERA, direct and resolved events have been identified by measuring the fraction $x_\gamma$ of the photon energy participating in the hard scattering in two-jet events [25]. The direct and resolved processes in $\gamma$p interactions correspond to the single-resolved (Fig. 2b) and double-resolved processes (Figs. 2d,f) in $\gamma\gamma$ interactions if the incoming proton is substituted in the place of a VMD-like photon. The direction of the photon remnant in $\gamma$p events is defined by the direction of the incoming electron beam. In $\gamma\gamma$ scattering the photons are emitted from both electrons, therefore a pair of variables is defined [26]

$$x_\gamma^+ = \frac{\sum_{\rm jets}(E+p_z)}{\sum_{\rm hadrons}(E+p_z)} \quad \text{and} \quad x_\gamma^- = \frac{\sum_{\rm jets}(E-p_z)}{\sum_{\rm hadrons}(E-p_z)}, \tag{3}$$

where $p_z$ is the momentum component along the $z$ axis of the detector and $E$ is the energy of the jets or hadrons. We use only two-jet events to calculate $x_\gamma^\pm$. Ideally, the total energy of the event is contained in the two jets for direct events without remnant jets, i. e. $x_\gamma^\pm = 1$, whereas for single-resolved events either $x_\gamma^+$ or $x_\gamma^-$ and for double-resolved events both $x_\gamma^\pm$ values are expected to be much smaller than one. The variables $x_\gamma^\pm$ are measured using all tracks and

calorimeter clusters that were used in the jet finding algorithm. In addition, the energies in the forward and the silicon tungsten calorimeters, which are not used for jet finding and for the energy flow distributions, are added in the denominator of Eq. 3. This improves the separation of direct and resolved events.

Figure 5 shows the number of two-jet events as a function of $x_\gamma^+$, together with the PYTHIA and PHOJET samples, after the detector simulation. The $x_\gamma^-$ distribution, which is not shown, is consistent with the $x_\gamma^+$ distribution within the statistical errors. The peak expected for direct and single-resolved events at $x_\gamma^+ = 1$ is smeared out due to higher order QCD effects such as $\gamma\gamma \to q\bar{q}g$ as well as hadronisation and detector resolution effects. Only statistical errors are shown, since systematic effects largely cancel in the ratio (Eq. 3), apart from the uncertainties on the hadronic energy scale of the forward and the silicon tungsten calorimeters which should affect data and Monte Carlo events in a similar way.

The direct events, which are shown separately for the PYTHIA sample, mainly contribute in the region $x_\gamma^+ > 0.8$. The number of two-jet events predicted by the PYTHIA simulation for $x_\gamma^+ < 0.8$ is too small, whereas the PHOJET simulation overestimates the number of two-jet events in almost all bins. Experimentally, samples with large and small direct contributions are separated by requiring $\min(x_\gamma^+, x_\gamma^-) > 0.8$ and $\min(x_\gamma^+, x_\gamma^-) < 0.8$, respectively. In the PYTHIA Monte Carlo 95 % of all events in the region $\min(x_\gamma^+, x_\gamma^-) > 0.8$ originate from direct interactions.

The transverse energy flow (Eq. 2) with respect to the jet direction is shown in Fig. 6 for two-jet events with $\min(x_\gamma^+, x_\gamma^-) < 0.8$ (low $x_\gamma$) and with $\min(x_\gamma^+, x_\gamma^-) > 0.8$ (high $x_\gamma$), separately. The rapidity difference in Eq. 2 is now multiplied by a factor $k = \pm 1$:

$$\Delta\eta' = k(\eta - \eta^{\text{jet}}).$$

The factor $k$ is chosen event-by-event to be $k = +1$ for events with $x_\gamma^+ > x_\gamma^-$ and $k = -1$ for events with $x_\gamma^+ < x_\gamma^-$. The definition of $\Delta\phi$ is unchanged. As a consequence, there is always more of the remnant at $\Delta\eta' < 0$ and the enhancement due to the additional transverse energy flow observed at negative and positive $\Delta\eta'$ is asymmetric. As expected, the enhancement in the region around $|\Delta\phi| \approx \pi/2$ and at $|\Delta\eta| > 1$ is more pronounced for low $x_\gamma$ events. The jets in high $x_\gamma$ events are much more back-to-back in $\Delta\phi$ (Fig. 6d) than in events with low $x_\gamma$ (Fig. 6c). The pedestal in the $\Delta\phi$ region between the two jets at $|\Delta\phi| \approx \pi/2$ is not observed in the events with high $x_\gamma$. As in Fig. 4 the Monte Carlo models underestimate the transverse energy flow in the central region around the jet axis. Jets in high $x_\gamma$ events are observed, on average, to have more average transverse energy and to be more collimated than low $x_\gamma$ events. This is as expected for direct events, where all the available energy is used in the hard subsystem.

# 7 Inclusive jet cross-sections

The inclusive one- and two-jet cross-sections in the range $|\eta^{\text{jet}}| < 1$ and $E_T^{\text{jet}} > 3$ GeV are measured using the cone jet finding algorithm (Section 5) with a cone size $R = 1$.

In order to obtain jet cross-sections which can be compared to theoretical calculations, we use the unfolding program RUN [27] to correct for the selection cuts, the resolution effects of

the detector and the background from non-signal processes. The generator jets serving as input to the unfolding procedure are found with the same jet algorithm as for the data, but using the energies and angles of primary hadrons (defined as all hadrons and photons after strong and electromagnetic decays) instead of those of tracks and calorimeter clusters. No additional corrections are applied for jet energy falling outside the cone or additional non-jet energy inside the cone. To improve the results of the unfolding program in the region $E_T^{\rm jet} > 3$ GeV, migration effects from jets at low $E_T^{\rm jet}$ must be taken into account. Therefore the jets are actually found with $E_T^{\rm min} = 2$ GeV and the unfolding is performed in the full $E_T^{\rm jet} > 2$ GeV range. The difference between the number of jets in the data with $E_T^{\rm jet} > 3$ GeV for $E_T^{\rm min} = 2$ GeV and $E_T^{\rm min} = 3$ GeV is less than the statistical uncertainty.

In Fig. 7, the inclusive one-jet cross-section for all jets is shown as a function of $E_T^{\rm jet}$. The error bars show the statistical and the systematic errors added in quadrature. The bin sizes, which are indicated by the vertical lines at the top of the figures, approximately reflect the experimental resolution. The determination of the average transverse energy $\langle E_T^{\rm jet} \rangle$ plotted on the abscissa is based on the method proposed in Reference [28]. The average $\langle E_T^{\rm jet} \rangle$ is obtained by integrating an exponential function which is fitted to the neighbouring data points. The error on $\langle E_T^{\rm jet} \rangle$ is calculated by varying the slope of the exponential function. The results are summarised in Table 2.

The systematic uncertainty on all jet cross-sections given in this section is determined by varying the energy scale of the ECAL in the Monte Carlo simulation by $\pm 5$ % and by degrading the resolution of the track parameters. An additional error comes from the unfolding procedure and from dependence on the Monte Carlo model used for unfolding. This model dependence is taken into account by adding to the systematic error the difference between the results obtained with PYTHIA, which are taken to be the central values, and PHOJET. The systematic error is smaller for the unfolding in $|\eta^{\rm jet}|$ than for the unfolding in $E_T^{\rm jet}$. Migration effects between bins have a large effect on the shape of the steeply falling $E_T^{\rm jet}$ distribution and its normalisation is dominated by the lowest $E_T^{\rm jet}$ bin near to the cut-off.

The $E_T^{\rm jet}$ distribution is compared to an NLO perturbative QCD calculation of the inclusive one-jet cross-section by Kleinwort and Kramer [4] who use the NLO GRV parametrisation of the photon structure function [15]. Their calculation was repeated for the kinematic conditions of this analysis. All scales are chosen to be equal to $E_T^{\rm jet}$. The strong coupling $\alpha_{\rm s}$ is calculated from the two-loop formula with $\Lambda^{(5)}_{\overline{\rm MS}} = 130$ MeV. The ratio of the NLO to the LO inclusive one-jet cross-section decreases from about 1.19 to 1.03 between $E_T^{\rm jet} = 3$ GeV and $E_T^{\rm jet} = 16$ GeV.

The direct, single- and double-resolved parts of the one-jet cross-section and their sum are shown separately. The agreement between data and the calculation is good. The resolved cross-sections dominate in the region $E_T^{\rm jet} \lesssim 5$ GeV, whereas, at high $E_T^{\rm jet}$ the direct cross-section is largest. The $E_T^{\rm jet}$ distribution is expected to fall less steeply than in $\gamma$p and $\overline{\rm p}$p interactions, because the fraction of hard interactions rises from $\overline{\rm p}$p (no direct and single-resolved processes) to $\gamma$p (no direct process) to $\gamma\gamma$ interactions.

It should be noted that the NLO QCD calculation gives the jet cross-section for massless partons, whereas the experimental jet cross-sections are measured for hadrons. The uncertainties due to the modelling of the hadronisation process have not been taken into account. Assuming perfect hadron-parton duality, no difference between hadron and parton level would

be observed. A correction of the hadronisation effects in the data is problematic, because the partons generated in the Monte Carlo and the partons used in the NLO calculation are not equivalent. The LO parton jets generated in PYTHIA before parton showering and fragmentation were compared with the hadron jets in order to estimate the effect of the correction. Only direct events which have no remnant jet were used for this comparison. The resulting correction would increase the cross-section by about a factor 1.2 to 1.3 in the range $E_T^{\rm jet} > 5$ GeV where the direct part of the cross-section dominates. This factor is of the same magnitude as the uncertainty of the measurement. These results are in qualitative agreement with the results of a similar study for jets in photoproduction [29].

About 16 % of the events contributing to the inclusive one-jet cross-section contain two jets. The invariant mass $M_{\rm jj}$ of the two-jet system is kinematically restricted to be $\gtrsim$4 GeV/$c^2$ by the $E_T^{\rm jet}$ cut. The average invariant mass $\langle M_{\rm jj} \rangle$ in the data is about 9 GeV/$c^2$.

The inclusive two-jet cross-section is measured using events with at least two jets. If an event contains more than two jets, only the two jets with the highest $E_T^{\rm jet}$ values are taken. The unfolding and the determination of the systematic uncertainties is done in the same way as for the inclusive one-jet cross-section. The differential inclusive two-jet cross-section as a function of $E_T^{\rm jet}$ is shown in Fig. 8. The cross-sections are given in Table 3. The $E_T^{\rm jet}$ distribution is also compared to the calculations by Kleinwort and Kramer [4] which have been extended to include the full NLO calculation for the double-resolved two-jet cross-section. The increase of the NLO compared to the LO inclusive two-jet cross-section is less than 10 % in their calculation.

The inclusive one-jet and two-jet cross-sections as a function of $|\eta^{\rm jet}|$ are shown in Figs. 9 and 10. The average $\langle \eta^{\rm jet} \rangle$ values are consistent with being at the centre of the bins. Within the statistical and systematic uncertainties of the measurement, the distributions are independent of $|\eta^{\rm jet}|$ in the kinematic range shown, in agreement with the expectations of some of the Monte Carlo models. This need not be taken to be the observation of a flat rapidity plateau in the $\gamma\gamma$ centre-of-mass system, since $\eta^{\rm jet}$ is defined in the laboratory system. There are strong smearing effects due to the Lorentz boost of the $\gamma\gamma$ system to the laboratory system, which varies on an event-by-event basis.

The total cross-sections, which are dominated by the low $E_T^{\rm jet}$ events, depend on the photon structure function. In Figs. 9 and 10, the total jet cross-sections predicted by the two Monte Carlo models differ significantly even if the same photon structure function (here SaS-1D) is used. This model dependence reduces the sensitivity to the parametrisation of the photon structure function. Different parametrisations were used as input to the PHOJET simulation. The GRV-LO and SaS-1D parametrisations describe the data equally well, but the LAC1 parametrisation [30] overestimates the total jet cross-section by about a factor of two.

# 8 Conclusions

We have measured jet production in photon-photon interactions with the OPAL detector at $e^+e^-$ centre-of-mass energies $\sqrt{s}_{\rm ee}$ of 130 and 136 GeV. Jets were identified using a cone jet finding algorithm with $R = 1$ in the kinematic range $E_T^{\rm jet} > 3$ GeV and $|\eta^{\rm jet}| < 1$.

Two-jet events originating from direct and resolved photon interactions were separated experimentally using the variables $x_\gamma^\pm$. Jets in events with $\min(x_\gamma^+, x_\gamma^-) > 0.8$ are expected to be produced mainly from direct photon interactions. These jets are observed to have, on average, more average transverse energy and to be more collimated than jets in resolved events with $\min(x_\gamma^+, x_\gamma^-) < 0.8$ . In resolved events a pedestal is observed in the transverse energy flows which may be related to the photon remnant. The Monte Carlo models PYTHIA and PHOJET describe the shape of the transverse energy flow distributions reasonably well.

The inclusive one-jet and two-jet cross-sections were measured as a function of $E_T^{\rm jet}$ and $|\eta^{\rm jet}|$. The measurement extends the $E_T^{\rm jet}$ range of previous measurements [5,6] up to $E_T^{\rm jet} = 16$ GeV. The $E_T^{\rm jet}$ dependent one- and two-jet cross-sections are in good agreement with next-to-leading order QCD calculations by Kleinwort and Kramer [4] which predict that the direct cross-section dominates at $E_T^{\rm jet} \gtrsim 5$ GeV.

Within the uncertainties of the measurements, the jet cross-sections are nearly independent of $|\eta^{\rm jet}|$ in the range $|\eta^{\rm jet}| < 1$. This should not be interpreted as an observation of a flat rapidity plateau in the $\gamma\gamma$ centre-of-mass system, since there are strong smearing effects due to the Lorentz boost of the $\gamma\gamma$ system to the laboratory system which varies on an event-by-event basis. The total jet production cross-section is dominated by the resolved cross-section in the low $E_T^{\rm jet}$ region. Large differences between the calculated jet cross-sections in PYTHIA and PHOJET reduce the sensitivity to the parametrisation of the photon structure function. Given this model dependence, the GRV-LO and SaS-1D parametrisations describe the data equally well. The LAC1 parametrisation overestimates the total jet cross-section by about a factor of two.

# Acknowledgements

We thank R. Engel and T. Sjöstrand for providing the Monte Carlo code and for many useful discussions and G. Kramer and T. Kleinwort for providing the NLO calculations.
We particularly wish to thank the SL Division for the efficient operation of the LEP accelerator at the new energies of $\sqrt{s}_{\rm ee} = 130+136$ GeV with good beam conditions and for their continuing close cooperation with our experimental group. In addition to the support staff at our own institutions we are pleased to acknowledge the
Department of Energy, USA,
National Science Foundation, USA,
Particle Physics and Astronomy Research Council, UK,
Natural Sciences and Engineering Research Council, Canada,
Israel Science Foundation, administered by the Israel Academy of Science and Humanities,
Minerva Gesellschaft,
Japanese Ministry of Education, Science and Culture (the Monbusho) and a grant under the Monbusho International Science Research Program,
German Israeli Bi-national Science Foundation (GIF),
Direction des Sciences de la Matière du Commissariat à l'Energie Atomique, France,
Bundesministerium für Bildung, Wissenschaft, Forschung und Technologie, Germany,
National Research Council of Canada,
Hungarian Foundation for Scientific Research, OTKA T-016660, and OTKA F-015089.

# References


[1] OPAL Collaboration, R. Akers et al., Z. Phys. C61 (1994) 199;
DELPHI Collaboration, P. Abreu et al., Z. Phys. C69 (1996) 223.

[2] C. H. Llewellyn Smith, Phys. Lett. B79 (1978) 83.

[3] P. Aurenche, J. Ph. Guillet, M. Fontannaz, Y. Shimizu, J. Fujimoto and K. Kato, Progr. Theor. Phys. 92 (1994) 175;
P. Aurenche, J. Ph. Guillet, M. Fontannaz, Y. Shimizu, J. Fujimoto and K. Kato, Proc. Workshop on Two-Photon Physics at LEP and HERA, Lund, Sweden (May 1994) 269.

[4] T. Kleinwort, G. Kramer, DESY-96-035 (1996);
T. Kleinwort, G. Kramer, Phys. Lett. B370 (1996) 141;
T. Kleinwort, G. Kramer, private communication.

[5] AMY Collaboration, B. J. Kim et al., Phys. Lett. B325 (1994) 248.

[6] TOPAZ Collaboration, H. Hayashii et al., Proc. 10th Workshop on Gamma-Gamma Collisions and Related Processes, Sheffield, UK (April 1995) 133;
TOPAZ Collaboration, H. Hayashii et al., Phys. Lett. B314 (1993) 149.

[7] T. Sjöstrand, Comp. Phys. Commun. 82 (1994) 74.

[8] R. Engel and J. Ranft, Phys. Rev. D54 (1996) 4244;
R. Engel, Z. Phys. C66 (1995) 203.

[9] DELPHI Collaboration, P. Abreu et al, Z. Phys. C62 (1994) 357.

[10] ALEPH Collaboration, D. Buskulic et al., Phys. Lett. B313 (1993) 509.

[11] For a general review see: H. Kolanoski, *Two-Photon Physics at $e^+e^-$ Storage Rings*, Springer-Verlag (1984).

[12] P. Kessler, Proc. Workshop on Two-Photon Physics at LEP and HERA, Lund, Sweden (May 1994) 183.

[13] G. A. Schuler and T. Sjöstrand, CERN-TH/96-119 and LU-TP-96-13;
G. A. Schuler and T. Sjöstrand, Nucl. Phys. B407 (1993) 539.

[14] G. A. Schuler and T. Sjöstrand, Z. Phys. C68 (1995) 607.

[15] M. Glück, E. Reya and A. Vogt, Phys. Rev. D46 (1992) 1973;
M. Glück, E. Reya and A. Vogt, Phys. Rev. D45 (1992) 3986.

[16] S. Jadach, B. F. L. Ward and Z. Was, Comp. Phys. Commun. 79 (1994) 503.

[17] J. A. M. Vermaseren, Nucl. Phys. B229 (1983) 347.

[18] J. Allison et al., Nucl. Instrum. Methods A317 (1992) 47.

[19] OPAL Collaboration, K. Ahmet et al., Nucl. Instrum. Methods A305 (1991) 275;
P. P. Allport et al., Nucl. Instrum. Methods A346 (1994) 476;
P. P. Allport et al., Nucl. Instrum. Methods A324 (1993) 34.

[20] B. E. Anderson et al., IEEE Transactions on Nuclear Science 41 (1994) 845.

[21] UA1 Collaboration, G. Arnison et al., Phys. Lett. B123 (1983) 115;
UA2 Collaboration, J. Alitti et al., Phys. Lett. B257 (1991) 232;
CDF Collaboration, F. Abe et al., Phys. Rev. D45 (1992) 1448.

[22] H1 Collaboration, S. Aid et al., Z. Phys. C70 (1996) 17;
H1 Collaboration, T. Ahmed et al., Nucl. Phys. B445 (1995) 195;
H1 Collaboration, I. Abt et al., Phys. Lett. B314 (1993) 436;
H1 Collaboration, T. Ahmed et al., Phys. Lett. B297 (1992) 205.

[23] ZEUS Collaboration, M. Derrick et al., DESY 96-094 (1996);
ZEUS Collaboration, M. Derrick et al., Phys. Lett. B348 (1995) 665;
ZEUS Collaboration, M. Derrick et al., Phys. Lett. B342 (1995) 417.

[24] OPAL Collaboration, R. Akers et al., Z. Phys. C63 (1994) 197.

[25] ZEUS Collaboration, M. Derrick et al., Phys. Lett. B322 (1994) 287;
H1 Collaboration, T. Ahmed et al., Nucl. Phys. B445 (1995) 195.

[26] L. Lönnblad and M. Seymour (convenors), $\gamma\gamma$ *Event Generators*, in "Physics at LEP2", CERN 96-01, eds. G. Altarelli, T. Sjöstrand and F. Zwirner, Vol. 2 (1996) 187.

[27] V. Blobel, DESY-84-118 (1984);
V. Blobel, Proc. 1984 CERN School of Computing, Aiguablava, Spain, CERN 85-09 (September 1984);
V. Blobel, *The RUN manual, Regularized Unfolding for High-Energy Physics Experiments*, program manual, unpublished.

[28] G. D. Lafferty and T. R. Wyatt, Nucl. Instrum. Methods A355 (1995) 541.

[29] M. Klasen, G. Kramer and S. G. Salesch, Z. Phys. C68 (1995) 113.

[30] H. Abramowicz, K. Charchula and A. Levy, Phys. Lett. B269 (1991) 458.

| | 0-jet | 1-jet | 2-jet | 3-jet | 4-jet |
|---|---|---|---|---|---|
| data | 6685 | 934 | 174 | 13 | 2 |
| $\gamma\gamma \to \tau\tau$ | $2.3 \pm 0.7$ | $2.3 \pm 0.7$ | $0.4 \pm 0.3$ | $< 0.3$ | $< 0.3$ |
| $e\gamma \to e$ + hadrons ($Q^2 > 0.8$ GeV$^2$) | $61.0 \pm 5.5$ | $3.0 \pm 1.2$ | $< 0.9$ | $< 0.9$ | $< 0.9$ |
| $e^+e^- \to (\gamma/Z^0)^* \to$ hadrons($\gamma$) | $7.1 \pm 0.6$ | $7.3 \pm 0.6$ | $3.5 \pm 0.4$ | $0.5 \pm 0.2$ | $0.1 \pm 0.1$ |
| $e^+e^- \to (\gamma/Z^0)^* \to \tau\tau(\gamma)$ | $0.04 \pm 0.01$ | $0.08 \pm 0.02$ | $0.09 \pm 0.02$ | $< 0.01$ | $< 0.01$ |

*Table 1: Number of n-jet events in the data and the expected contribution from the main background processes.*

| $E_T^{\rm jet}$ (GeV) | $\langle E_T^{\rm jet} \rangle$ (GeV) | $d\sigma/dE_T^{\rm jet}$ (pb/GeV) | $\lvert\eta^{\rm jet}\rvert$ | $d\sigma/d\lvert\eta^{\rm jet}\rvert$ (pb) |
|---|---|---|---|---|
| 3.0– 4.0 | $3.45 \pm 0.02$ | $163.4 \pm 5.8 \pm 26.7$ | 0.0 – 0.25 | $277 \pm 16 \pm 27$ |
| 4.0– 5.0 | $4.46 \pm 0.01$ | $36.0 \pm 2.3 \pm 7.7$ | 0.25 – 0.50 | $262 \pm 15 \pm 29$ |
| 5.0– 6.5 | $5.70 \pm 0.03$ | $18.0 \pm 1.5 \pm 3.6$ | 0.50 – 0.75 | $228 \pm 12 \pm 32$ |
| 6.5– 8.5 | $7.41 \pm 0.04$ | $8.4 \pm 1.0 \pm 1.8$ | 0.75 – 1.0 | $240 \pm 13 \pm 56$ |
| 8.5–11.0 | $9.64 \pm 0.08$ | $1.8 \pm 0.3 \pm 0.5$ | | |
| 11.0–16.0 | $13.14 \pm 0.11$ | $0.78 \pm 0.17 \pm 0.24$ | | |

*Table 2: The inclusive one-jet cross-section. The first error is statistical and the second error is systematic.*

| $E_T^{\rm jet}$ (GeV) | $\langle E_T^{\rm jet} \rangle$ (GeV) | $d\sigma/dE_T^{\rm jet}$ (pb/GeV) | $\lvert\eta^{\rm jet}\rvert$ | $d\sigma/d\lvert\eta^{\rm jet}\rvert$ (pb) |
|---|---|---|---|---|
| 3.0– 4.0 | $3.46 \pm 0.02$ | $36.0 \pm 2.9 \pm 4.2$ | 0.0 – 0.25 | $67 \pm 7 \pm 11$ |
| 4.0– 5.0 | $4.47 \pm 0.01$ | $18.4 \pm 2.0 \pm 3.5$ | 0.25 – 0.50 | $92 \pm 9 \pm 12$ |
| 5.0– 6.5 | $5.70 \pm 0.03$ | $8.7 \pm 1.1 \pm 0.8$ | 0.50 – 0.75 | $74 \pm 8 \pm 9$ |
| 6.5– 8.5 | $7.41 \pm 0.04$ | $3.7 \pm 0.6 \pm 1.4$ | 0.75 – 1.0 | $72 \pm 8 \pm 12$ |
| 8.5–11.0 | $9.65 \pm 0.10$ | $1.13 \pm 0.28 \pm 0.34$ | | |
| 11.0–16.0 | $13.16 \pm 0.20$ | $0.32 \pm 0.09 \pm 0.17$ | | |

*Table 3: The inclusive two-jet cross-section. The first error is statistical and the second error is systematic.*

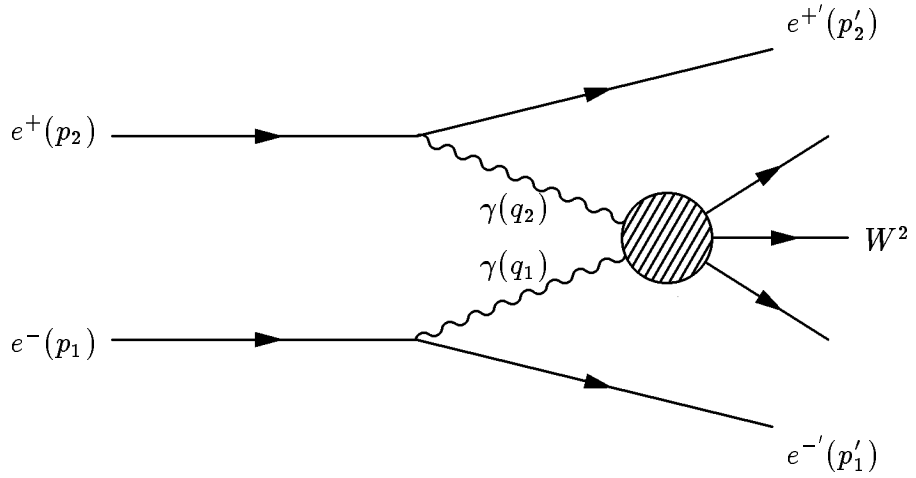


*Figure 1: Diagram of a two-photon scattering process.*

**Direct:**

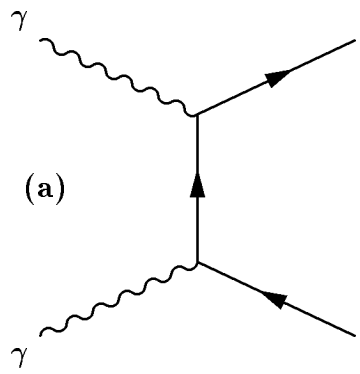


**Single-Resolved:**

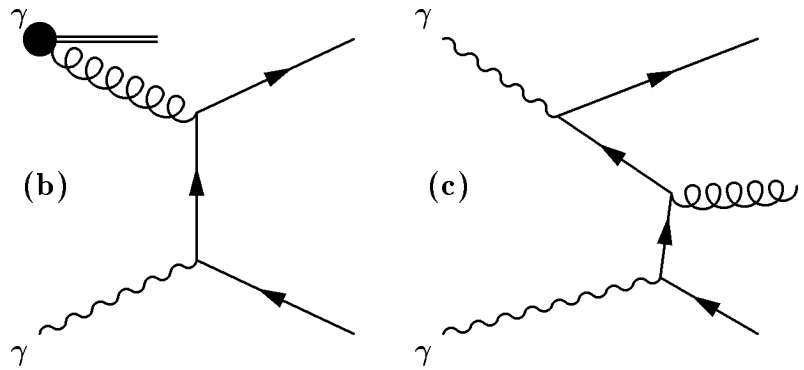


**Double-Resolved:**

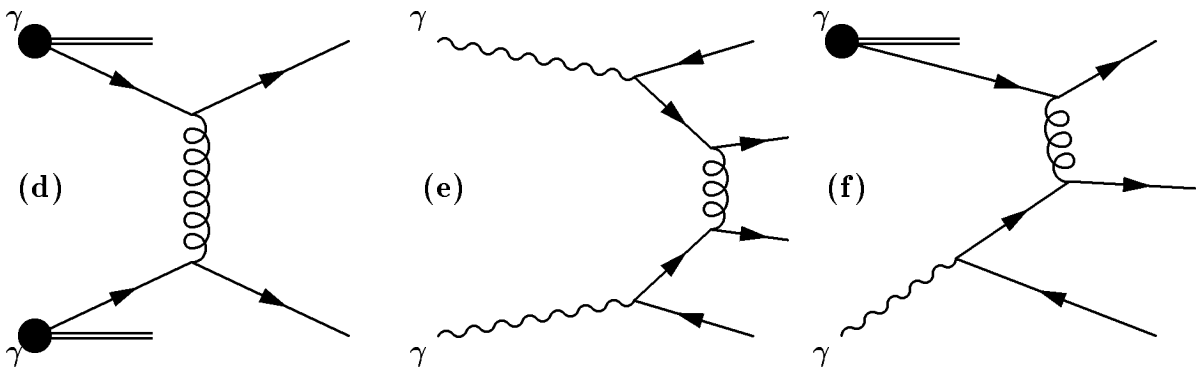


*Figure 2: All combinations of photon components simulated in PYTHIA. The partons which can lead to hard jets are shown as full lines, whereas the double lines represent the photon remnants in the VMD interactions. Not all possible processes are shown. The parton processes used in the matrix element calculation for the examples shown are given in parentheses:*
**a***: direct* $\times$ *direct* ($\gamma\gamma \to q\overline{q}$)*;*
**b***: VMD* $\times$ *direct* ($g\gamma \to q\overline{q}$)*;* **c***: anomalous* $\times$ *direct* ($\overline{q}\gamma \to g\overline{q}$)*;*
**d***: VMD* $\times$ *VMD;* **e***: anomalous* $\times$ *anomalous;* **f***: VMD* $\times$ *anomalous (all* $qq \to qq$*).*

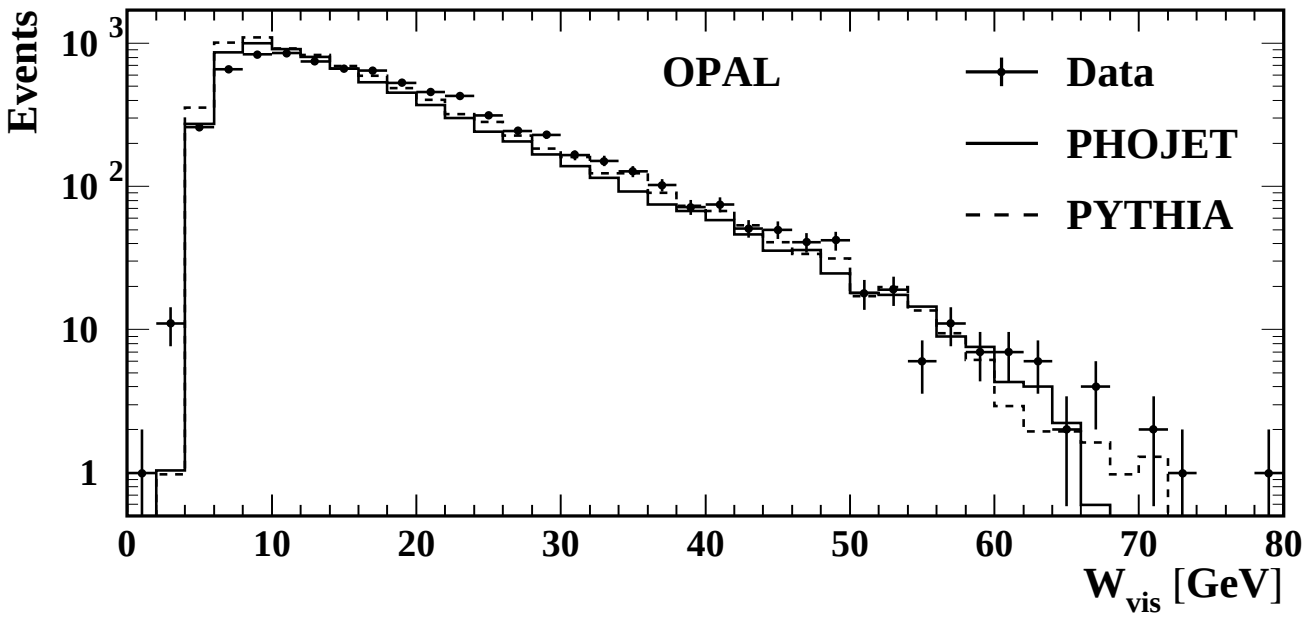


*Figure 3: The distribution of the visible hadronic invariant mass $W_{vis}$ for all selected events compared to the PHOJET (continuous line) and PYTHIA (dashed line) simulations. Statistical errors only are shown.*

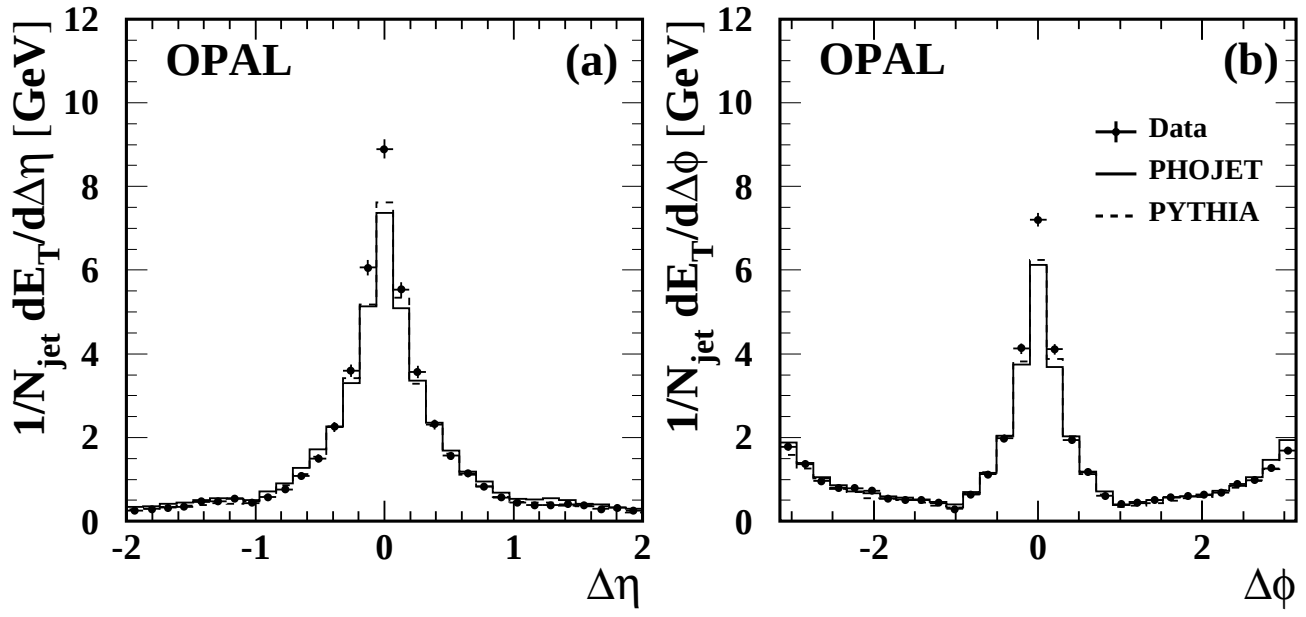


*Figure 4: Uncorrected energy flow transverse to the beam direction measured relative to the jet directions for all jets. The energy flow is integrated over $|\Delta\phi| < \pi/2$ for the $\Delta\eta$ projection (a) and over $|\Delta\eta| < 1$ for the $\Delta\phi$ projection (b). Statistical errors only are shown. The data (dots) are compared to the PHOJET (continuous line) and PYTHIA (dashed line) simulations.*

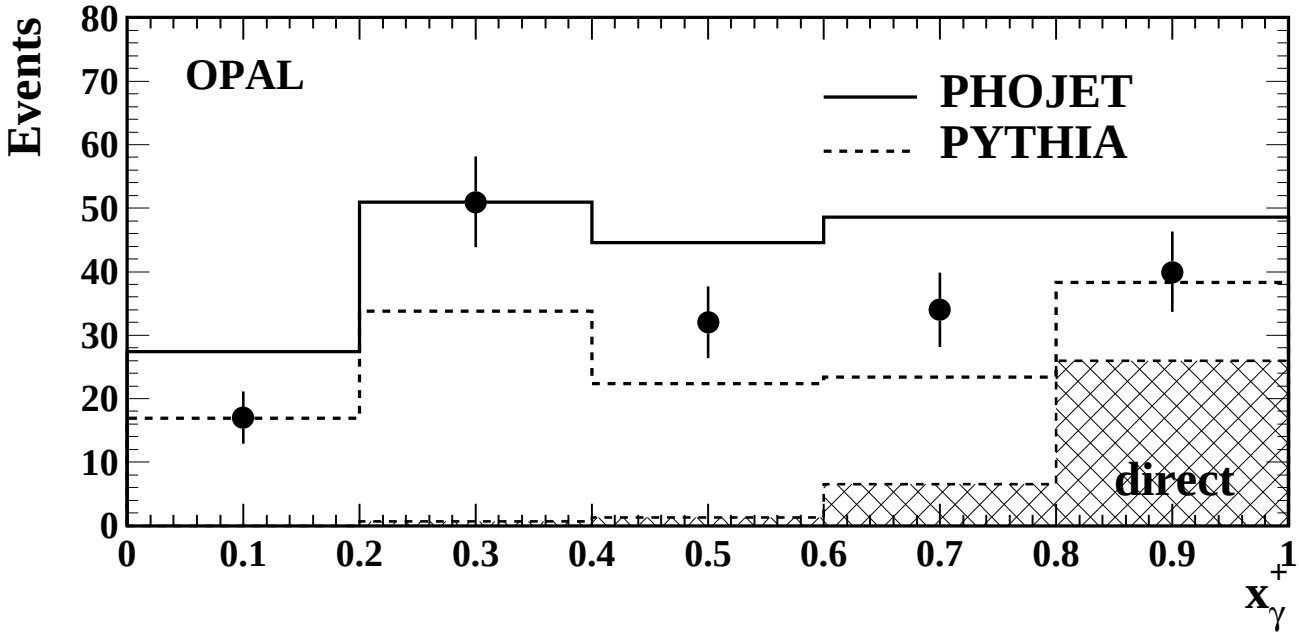


*Figure 5: The number of two-jet events as a function of $x_\gamma^+$ compared to PHOJET (continuous line) and PYTHIA (dashed line). Statistical errors only are shown and the data points are plotted at the centre of the bins. The hatched histogram is the direct contribution to the PYTHIA events.*

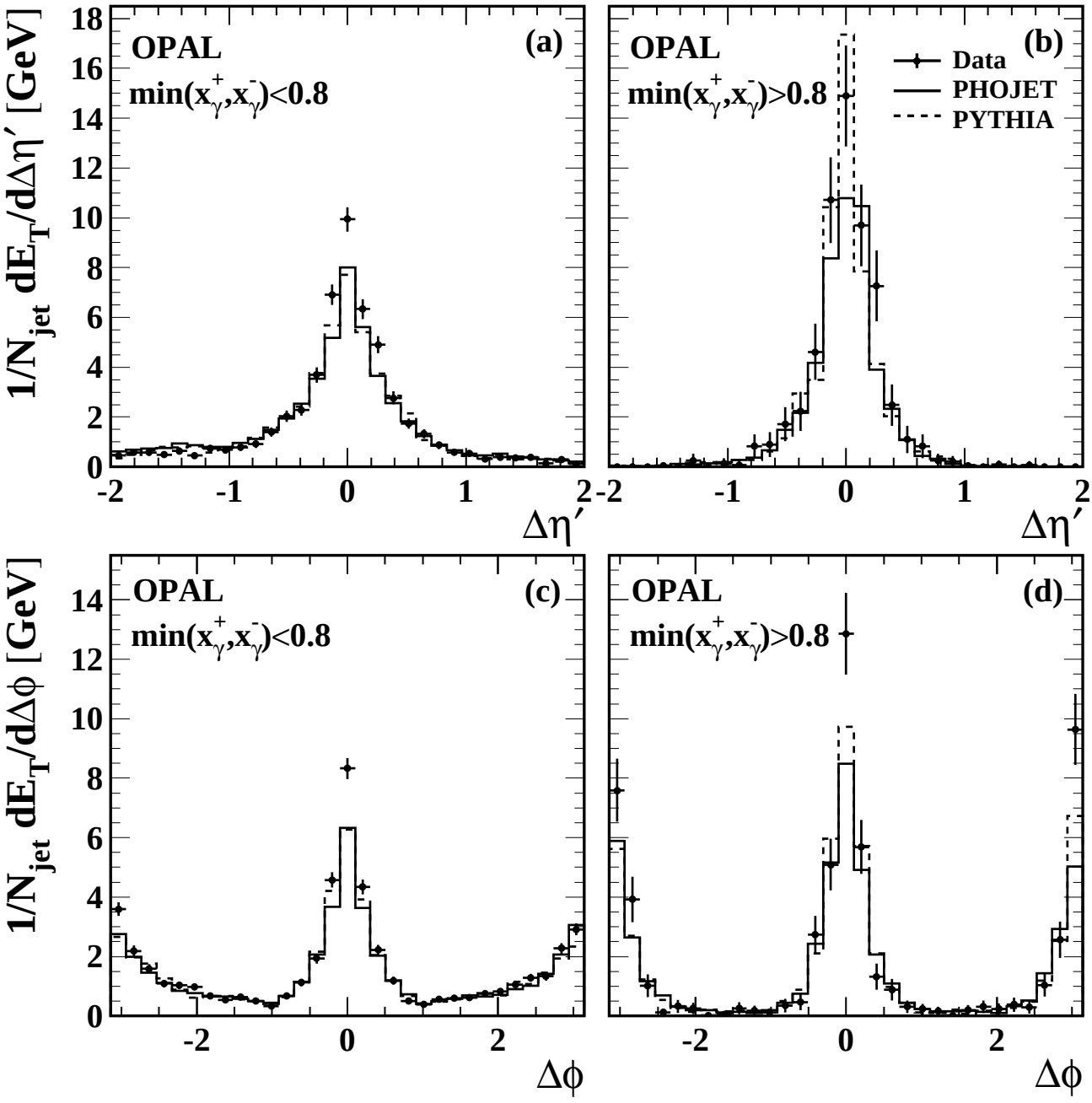


*Figure 6: Uncorrected energy flow transverse to the beam direction measured relative to the direction of each jet in two-jet events. Jets from events with* $\min(x_\gamma^+, x_\gamma^-) < 0.8$ *(a,c) and* $\min(x_\gamma^+, x_\gamma^-) > 0.8$ *(b,d) are shown separately. The energy flow is integrated over* $|\Delta\phi| < \pi/2$ *for the* $\Delta\eta'$ *projection (a,b) and over* $|\Delta\eta'| < 1$ *for the* $\Delta\phi$ *projection (c,d). Statistical errors only are shown. The data (dots) are compared to the PHOJET (continuous line) and PYTHIA (dashed line) simulations.*

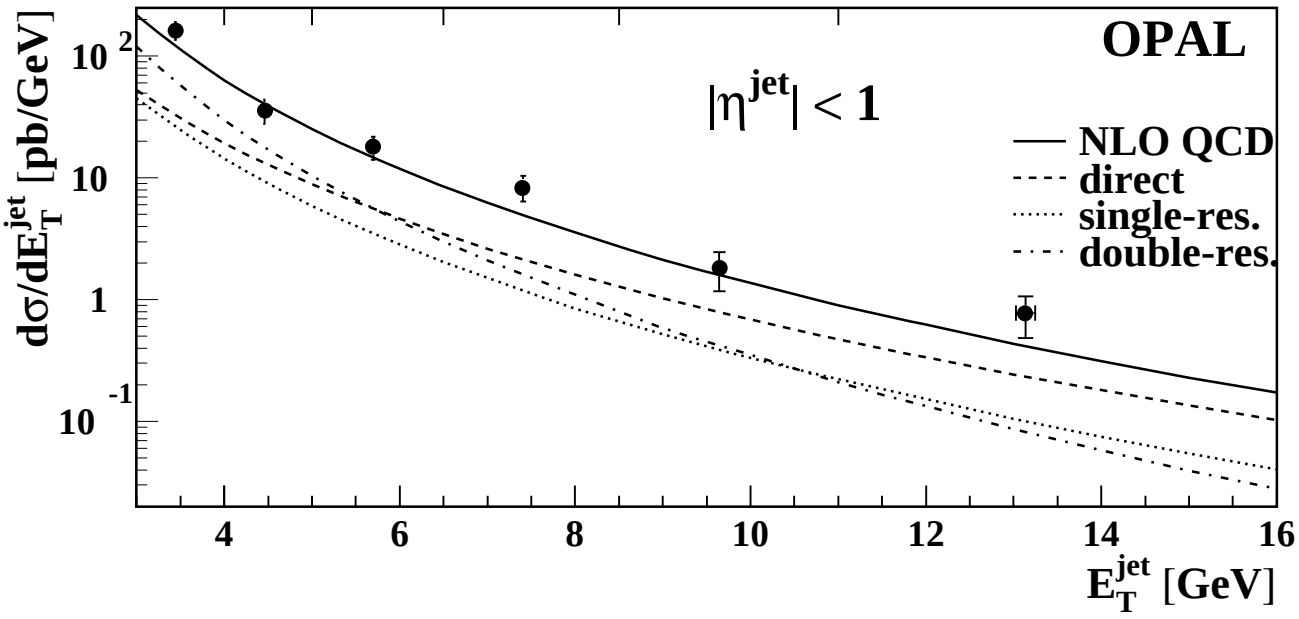


*Figure 7: The inclusive one-jet cross-section as a function of $E_T^{\rm jet}$ for jets with $|\eta^{\rm jet}| < 1$ compared to the NLO calculation by Kleinwort and Kramer [4]. The direct, single-resolved and double-resolved cross-sections and the sum (continuous line) are shown separately.*

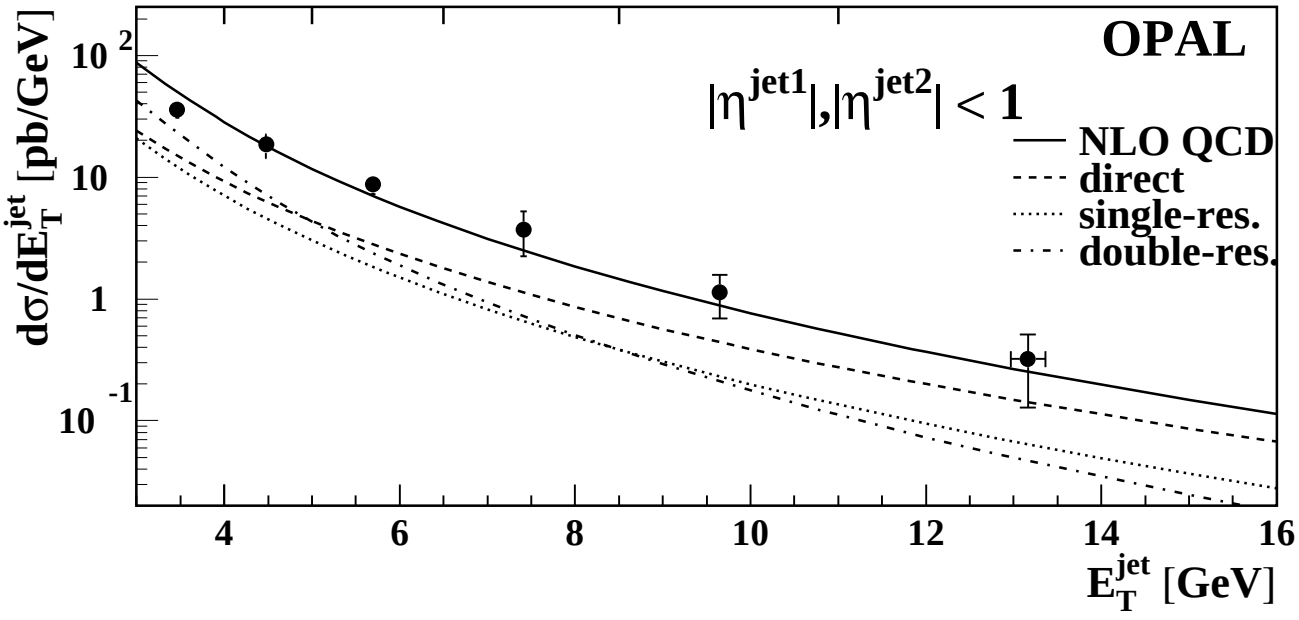


*Figure 8: The inclusive two-jet cross-section as a function of $E_T^{\rm jet}$ for jets with $|\eta^{\rm jet}| < 1$ compared to the NLO calculation by Kleinwort and Kramer [4]. The direct, single-resolved and double-resolved cross-sections and the sum (continuous line) are shown separately.*

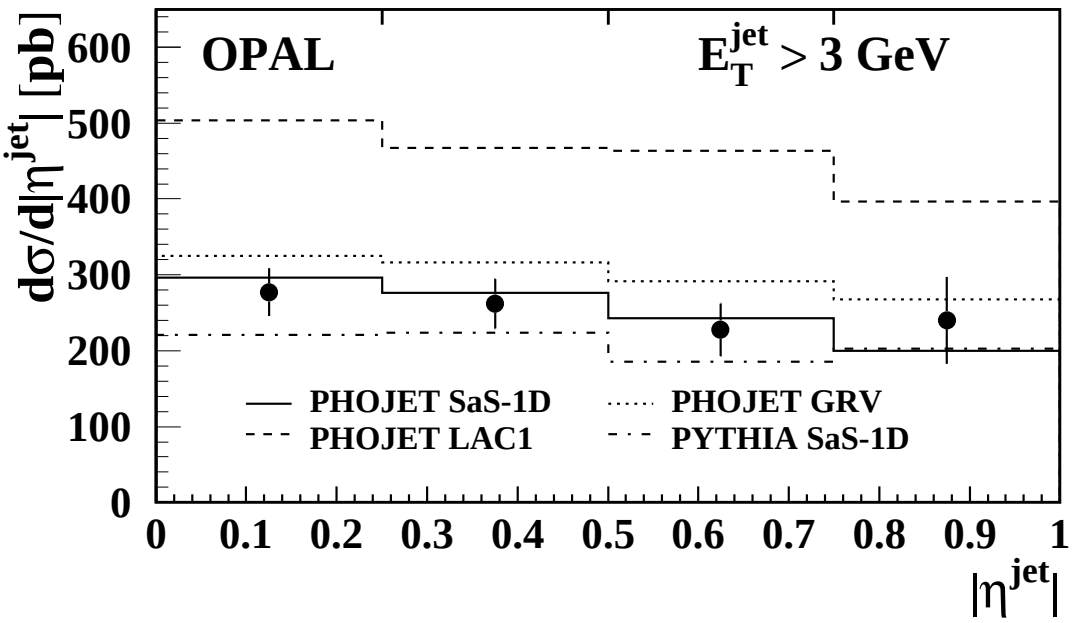


*Figure 9: The inclusive one-jet cross-section as a function of $|\eta^{\rm jet}|$ for jets with $E_T^{\rm jet} > 3$ GeV compared to the LO QCD calculations of PYTHIA and PHOJET.*

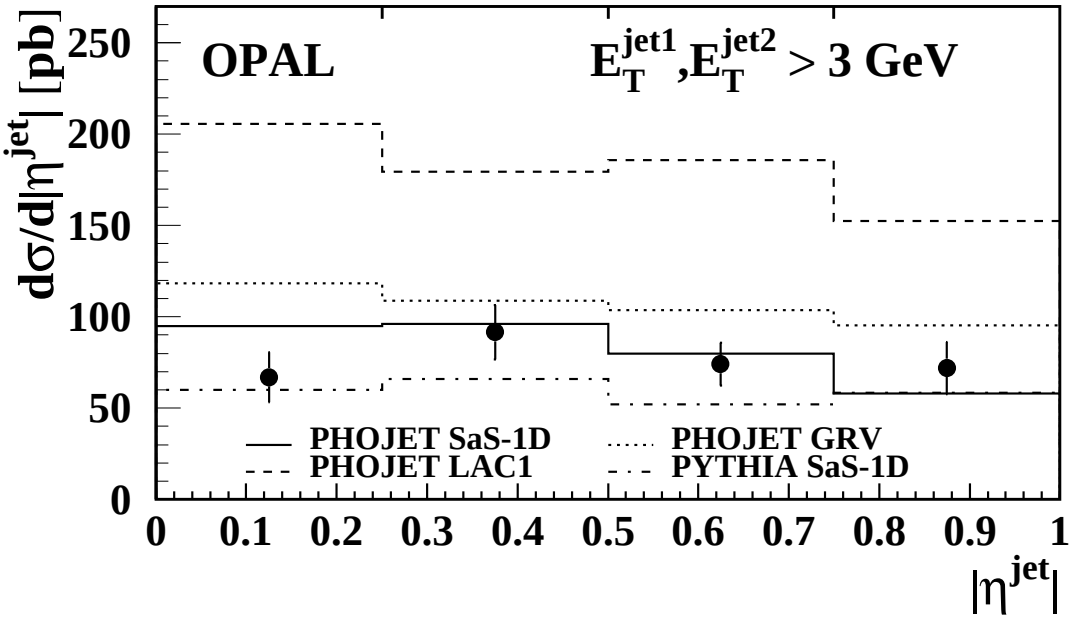


*Figure 10: The inclusive two-jet cross-section as a function of $|\eta^{\rm jet}|$ for jets with $E_T^{\rm jet} > 3$ GeV compared to the LO QCD calculations of PYTHIA and PHOJET.*